High-pressure structure and bonding in CaIrO$_3$: The structure model of MgSiO$_3$ post-perovskite investigated with time-of-flight neutron powder diffraction

C. DAVID MARTIN,[1,*] RONALD I. SMITH,[2] WILLIAM G. MARSHALL,[2] AND JOHN B. PARISE[1,3]

[1]Geosciences Department, 255 Earth and Space Sciences Building, Stony Brook University, Stony Brook, New York 11794-2100, U.S.A.
[2]ISIS Neutron Facility, Rutherford Appleton Laboratory, Chilton, Didcot, Oxon OX11 0QX, U.K.
[3]Chemistry Department, Stony Brook University, Stony Brook, New York 11794-3400, U.S.A.

ABSTRACT

The structure of CaIrO$_3$ (*Cmcm*) has been refined at high pressure and at low temperature using time-of-flight neutron powder diffraction data. Evidence supporting deviation from space group *Cmcm* to *Cmc*2_1 is inconclusive. As CaIrO$_3$ (*Cmcm*) unit-cell volume changes, refinements indicate deformation of cation-centered coordination polyhedra, rather than tilting. Structure models demonstrate Ca^{2+}-centered polyhedra are an order of magnitude more compressible than Ir^{4+}-centered octahedra. Bond valence sums show significant chemical strain (over-bonding) of calcium and oxygen at ambient conditions. Implications for structure change in MgSiO$_3$ post-perovskite are discussed and a method for predicting the Clapeyron slope between perovskite and post-perovskite phases is proposed based on extrapolation of the volume-ratio between cation-centered polyhedra.

Keywords: Post-perovskite, high pressure, structure, neutron diffraction, Rietveld refinement, bond valence, D″ layer, CaIrO$_3$

INTRODUCTION

MgSiO$_3$ perovskite (*Pbnm*) is expected to dominate the mineralogy of Earth's lower mantle, yet recent investigations of this high-pressure mineral find a phase transition to a post-perovskite structure at extreme conditions consistent with the depth of the D″ seismic discontinuity (Garnero 2004; Hirose 2006; Murakami et al. 2004; Oganov and Ono 2004). At the bottom of the mantle and just above Earth's metallic core, the D″ layer mediates chemical and heat exchange across the core-mantle boundary (Lay et al. 2004; Spera et al. 2006; Stixrude and Karki 2005). Knowledge of the structure and dynamics of this region as well as physical properties of MgSiO$_3$ post-perovskite are required to understand anomalous seismic observations of this region (Kubo et al. 2006; Lay et al. 1998, 2006; Mao et al. 2006; Merkel et al. 2006; Shieh et al. 2006; Sinmyo et al. 2006; Tsuchiya et al. 2005).

The post-perovskite MgSiO$_3$ structure has been observed in several ABX$_3$ and A$_2$X$_3$ materials at high pressure and appears consistent with the CaIrO$_3$ (*Cmcm*) structure model (Fig. 1). However, due to the extreme conditions required to stabilize post-perovskite phases, in situ investigations of its crystal structure utilize the diamond-anvil cell that significantly restricts powder sample volume and angular range of X-ray diffraction. As a result, textures often develop within powder samples and spherical harmonic preferred orientation corrections are applied during Rietveld structure refinement (Hirose et al. 2005; Kubo et al. 2006; Martin et al. 2006b; Santillan et al. 2006). Because significant correlations between parameters describing preferred orientation and crystal structure may exist when data are limited in angular range, structure details, changes, and mechanisms ac-commodating compression and thermal expansion will become clearer when data can be collected from samples free from preferred orientation.

CaIrO$_3$ (*Cmcm*) is the only oxide to exhibit this rare structure type at ambient conditions, however, some sulfides and high-Z halides adopt the CaIrO$_3$-type structure (Berndt 1997), suggesting the covalent nature of bonding in these materials is responsible for stability. The CaIrO$_3$ structure consists of isolated layers of IrO$_6$ octahedra normal to the **b** axis (Fig. 1), with these octahedra sharing edges along the **a** axis and corners along the **c** axis (Rodi and Babel 1965). Calcium occupies bi-capped trigonal prism sites between these layers. Since the structure of CaIrO$_3$ was discovered and characterized, the material has been the subject of relatively few studies, though previous investigations find a phase transition to the perovskite (*Pbnm*) structure-type at high temperature (Hirose and Fujita 2005; McDaniel and Schneider 1972). Several studies have investigated the room-pressure CaO-IrO$_2$ phase diagram in air, finding CaIrO$_3$ stable to ~1020 °C (McDaniel and Schneider 1972; Rodi and Babel 1965). However, recent work (Martin et al. 2007a) challenges these reports, concluding CaIrO$_3$ is metastable at 1 bar in air and only temporarily synthesized at room pressure when a (CaO + IrO$_2$) mixture is fired. Instead it is found that heating CaIrO$_3$ leads to (Ca$_2$IrO$_4$ + IrO$_2$) dissociation products and synthesis of pure CaIrO$_3$ powder requires high pressure. Volatilization of iridium in air via gaseous hydrates and IrO$_3$ (Eichler et al. 1993) might play a role in destabilizing CaIrO$_3$.

A recent structure investigation using X-ray diffraction finds compression of the unit cell of CaIrO$_3$ is significantly anisotropic (Martin et al. 2007a). Consistent with observations of MgGeO$_3$ post-perovskite (Hirose et al. 2005; Kubo et al. 2006), lattice planes normal to the **b** axis are compressed more readily than
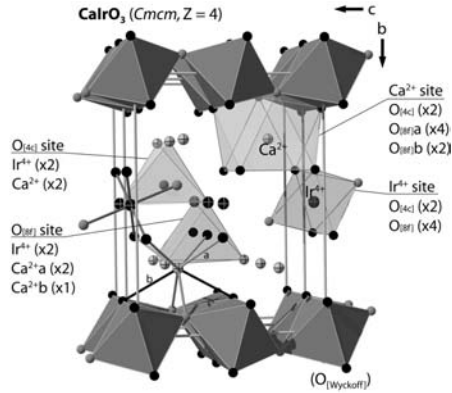

FIGURE 1. Structure model of CaIrO$_3$ (*Cmcm*), showing coordination environment of each ion site. Calcium (white sphere with cross) and iridium (black sphere with cross) cations are shown with each oxygen site designated by the Wyckoff position symbol 4*c* (gray sphere) or 8*f* (black sphere). The number of each unique bond belonging to each ion environment is listed for clarity.

those normal to **a** and **c** axes, respectively ($\beta_b > \beta_a > \beta_c$). However, Martin et al. (2007) find that although the thermal expansion of CaIrO$_3$ is dominated by expansion along **b**, the **c** axis expands more readily than the **a** axis, thus $\alpha_b > \alpha_c > \alpha_a$. This observation raises questions regarding the structural mechanism of compression and thermal expansion in CaIrO$_3$ in comparison with perovskite-type structures, where compression and thermal expansion of the unit cell are more isotropic and is commonly understood in terms of octahedral tilts and bond length changes (Zhao et al. 1993).

Previous work examining perovskite structured NaMgF$_3$ (ABX$_3$) indicates the volume ratio between A- (sodium-centered, V_A) and B-site (magnesium-centered, V_B) polyhedra is an indicator that may be used to predict the pressure-temperature region where the phase transition to post-perovskite structure may occur (Martin et al. 2006b). The V_A/V_B ratio decreases from 5 in high temperature NaMgF$_3$ perovskite (Thomas 1998) to ~4 at the phase boundary between high pressure room-temperature perovskite (*Pbnm*) and post-perovskite (*Cmcm*) structures (Martin et al. 2006b). Examining the V_A/V_B values in published post-perovskite phases, MgSiO$_3$, 4.01 (Murakami et al. 2004), 3.92 (Oganov and Ono 2004); NaMgF$_3$, 3.94(6) (Martin et al. 2006b); MgGeO$_3$, 4.28 (Hirose et al. 2005), 3.59 (Kubo et al. 2006); CaIrO$_3$, 4.19 (Rodi and Babel 1965); Fe$_2$O$_3$, 3.89 (Ono and Ohishi 2005); Mn$_2$O$_3$, 4.01 (Santillan et al. 2006), careful consideration of the V_A/V_B role on the perovskite/post-perovskite phase transition is warranted. Rietveld structure refinement of CaIrO$_3$ finds that V_A/V_B increases with temperature (Martin et al. 2007a) and this parameter could assist a structure-based understanding of the positive Clapeyron slope between perovskite and post-perovskite phases of MgSiO$_3$ if V_A/V_B should decrease with pressure.

To extract differences between structure models under changing pressure conditions, we utilize Rietveld structure refinement with neutron powder diffraction since these data are sensitive to oxygen as well as most cations in a material. From a synthesis of the data presented in this study, we identify mechanisms controlling structure changes in CaIrO$_3$ that may prove useful to an understanding of the elastic, rheological, and chemical properties of post-perovskite MgSiO$_3$.

EXPERIMENTAL METHODS

Using a piston-cylinder high pressure apparatus, CaIrO$_3$ was synthesized from a stoichiometric mixture of (Ca$_2$IrO$_4$ + IrO$_2$) at 2.0(1) GPa and 1150(75) K in a silver capsule surrounded by a ½ inch talc assembly. These conditions were sustained for 48 h prior to quenching to room temperature. The resultant sample was found to contain ~96(1) wt% CaIrO$_3$ with quantities of unreacted Ca$_2$IrO$_4$ and IrO$_2$. The initial (Ca$_2$IrO$_4$ + IrO$_2$) mixture was prepared by firing an equal-molar quantity of CaCO$_3$ and IrO$_2$ (Alfa Aesar; Lot no. E27P20) in a furnace at 850 °C for 48 h in air with iridium metal foil present in the covered Au crucible to buffer possible gaseous phases (Eichler et al. 1993). Because platinum and iridium alloy, platinum was not used during sample preparation.

Time-of-flight neutron powder diffraction data were collected on the POLARIS diffractometer at the ISIS pulsed spallation source Rutherford Appleton Laboratory, U.K. (Hull et al. 1992). For ambient pressure measurements, cylindrical pellets (~4 mm diameter × 2 mm high) were stacked in a thin-walled vanadium sample can and diffraction data were collected at room temperature, ~293 K, for 780 µAh proton beam current (~5 h). For measurements below room temperature the sample, in the same sample can, was loaded into a helium flow cryostat and diffraction patterns collected at 2, 100, and 250 K for between 1170 and 1250 µAh proton beam current (~7 h). Data from the highest resolution, backscattering, detector bank <2θ> = 145° were used in Rietveld profile refinement. Time-of-flight neutron powder diffraction patterns were collected from CaIrO$_3$ at high pressure using a type V2 Paris-Edinburgh press equipped with single profile WC/Ni binder-cored anvils in conjunction with the POLARIS 2θ = 90° detectors. The sample was confined within a null scattering TiZr capsule gasket (Marshall and Francis 2002) with the powder moistened with deuterated methanol:ethanol (4:1) pressure transmitting medium. Diffraction data were collected from the sample at hydraulic ram pressures of 70, 250, 500, 700, 850, and 800 bar, in sequential order. Judging by the bar/GPa trend and data trends with pressure, quasi-hydrostatic sample conditions were reached at 850 oil bars and data collected subsequently at 800 oil bar is considered representative of hydrostatic pressure conditions on the sample. Sample pressure was calculated using the known equation of state of CaIrO$_3$, with bulk modulus 180.2(28) GPa (Martin et al. 2007a).

Rietveld structure refinements were performed using the GSAS program suite (Larson and Von Dreele 2000) and the user interface EXPGUI (Toby 2001). While data were corrected for absorption according to the scattering cross-sections and relative abundances of each element, an additional correction was applied to data collected at high pressure according to neutron attenuation of the WC anvils of the Paris-Edinburgh press. Because of the significant neutron absorption of iridium and some uncertainty of the dependence on the instrumental absorption correction, isotropic displacement parameters calculated from high-pressure data are overestimated.

Estimated uncertainties on refined parameters are included within our figures as gray areas and these are obtained from error propagation (Goodman 1960) using the relation:

$$\text{for function } Z(y, x, ...),\ \sigma_Z = \sqrt{\left(\frac{\partial Z}{\partial y} * \sigma_y\right)^2 + \left(\frac{\partial Z}{\partial x} * \sigma_x\right)^2 + \left(\frac{\partial Z}{\partial ...} * \sigma...\right)^2}$$

where standard deviation (σ) is obtained directly from GSAS and/or through fitting.

RESULTS AND DISCUSSION

The refined unit-cell parameters, atomic positions, and displacement parameters of CaIrO$_3$ at 1 bar pressure in space group *Cmcm* are listed in Table 1 at 2.0(1), 100.0(1), 250.0(1), and 293(2) K. Within error, relative length changes of each unit cell axis in this temperature range are consistent with those occurring at higher temperatures (Martin et al. 2007a) and while small, thermal expansion at low temperature is dominated by expansion in the [010] direction.

Bond valence (Brown and Altermatt 1985; Brown and Shannon 1973) provides a basis from which we may understand Rietveld structure models of CaIrO$_3$ at ambient conditions in terms of ideal ionic bonding. In Pauling's ionic bonding model, all bonds between ions imply a charge-sum, which may be compared to the ionic charge (formal valence) of the ion. This is expressed mathematically as:

TABLE 1. Refined unit-cell parameters, atomic coordinates, isotropic temperature factors (*U*), and refinement statistics are listed for CaIrO₃ (*Cmcm*) at several low temperatures in section (**a**), while the residual bond strain value (*GII*) of the structure, experimental bond valence sums (*S*$_{ij}$), and chemical strain (*P*$_i$) of each ion are listed at room temperature in section (**b**)

(a) Temperature (K)	2.0(1)	100.0(1)	205.0(1)	293(2)
a (Å)	3.13451(9)	3.13493(8)	3.13622(9)	3.13645(5)
b	9.87568(27)	9.87709(27)	9.88198(28)	9.88352(15)
c	7.29518(18)	7.29562(17)	7.29871(18)	7.29903(10)
V (Å³)	225.825(10)	225.901(10)	226.202(11)	226.264(6)
Ca				
y	0.25019(13)	0.25019(13)	0.25034(15)	0.25035(9)
U (Å²·100)	0.185(13)	0.219(13)	0.343(15)	0.576(10)
Ir				
U	0.113(6)	0.141(6)	0.185(7)	0.251(4)
O$_{[4c]}$				
y	0.42541(12)	0.42539(12)	0.42551(13)	0.42505(7)
U	0.217(12)	0.238(12)	0.303(14)	0.428(9)
O$_{[8f]}$				
y	0.12692(8)	0.12679(8)	0.12667(9)	0.12719(5)
z	0.05064(10)	0.05046(10)	0.05025(11)	0.05036(6)
U	0.192(8)	0.218(8)	0.280(9)	0.383(6)
χ^2	1.471	1.334	1.194	1.798
wR$_P$	0.78%	0.74%	0.73%	2.06%
R$_P$	2.35%	2.21%	2.14%	6.25%

(b) *T* (K)	293(2)	Ca	Ir	O$_{[4c]}$	O$_{[8f]}$
S$_{ij}$ (v.u.)		2.26(5)	4.03(9)	−2.27(5)	−2.01(4)
P$_i$ (%)		13.0(24)	0.8(22)	13.7(24)	0.5(22)
*R*1 = 0.19(2)					

Notes: Ca = 0, *y*, 0; Ir = 0, 0, 0; O$_{4c}$ = 0, *y*, 0.25; O$_{8f}$ = 0, *y*, *z*. *wR*$_P$ = 100%·[Σ*w*(*I*$_O$ – *I*$_C$)²/ Σ*wI*$_O$²]$^{1/2}$. *R*$_P$ = 100%·Σ|*I*$_O$ – *I*$_C$|/Σ*I*$_O$². Terms *I*$_O$ and *I*$_C$ are observed and calculated profile intensities and *w* is weight associated with *I*$_O$.

$$V_i = \sum_j S_{ij}$$

where V_i is the formal valence of ion "I" and S_{ij} is the "bond strength," which is defined in terms of bond length (Brown and Altermatt 1985; Brown and Shannon 1973) as:

$$S_{ij} = \exp\left(\frac{R_0 - R_{ij}}{B}\right).$$

Thus, the bond strength is proportional to bond length and, for every bond between ions (R_{ij}), a standard distance (R_0) has been determined from systematic studies of crystal structures. The R_0 value for each bond must be known and the Ca²⁺-O value, 1.967(2) Å (Brown and Altermatt 1985), is better constrained than Ir⁴⁺-O, 1.87(1) Å (Wills and Brown 1999). The term *B* rarely deviates from 0.37 Å, and we assume uncertainty ±0.01 Å.

Bond valence sums of each ion in room temperature CaIrO₃ structure are listed in Table 1 and while V_{Ir} and $V_{O[8f]}$ are in good accord with 4⁺ and 2⁻, both V_{Ca} and $V_{O[4c]}$ deviate significantly from 2⁺ and 2⁻, respectively. Deviations from formal ion valence are considered using the simple difference:

$$d_i = \sum_j S'_{ij} - |V_i|$$

where S'_{ij} is the experimentally determined bond strength. It is useful to normalize deviations as a percentage (P_i) in terms of the formal ion valence:

$$P_i = \frac{d_i}{|V_i|} * 100\%$$

Difference between the experimental valence sum and the

formal ion valence is known as "chemical strain" (Brown 1992; Salinas-Sanchez et al. 1992) and positive percentages imply overbonding. At room temperature, P_{Ir}, P_{Ca}, $P_{O[4c]}$, and $P_{O[8f]}$ in CaIrO₃ are approximately 1, 13, 13, and 1, respectively. Previous work (Brown 1992; Salinas-Sanchez et al. 1992) has developed a general measure to classify overall chemical strain in crystalline materials:

$$GII = \sqrt{\left\langle d_i^2 \right\rangle}$$

The root-mean-square of valence difference values for each ion site in a particular structure is referred to as the "residual bond strain" or "global instability index." Our data indicate CaIrO₃ has a *GII* value of 0.16(2) valence units (dimensionless) at room temperature. Previous work finds *GII* > 0.1 in structures with significant residual bond strain and *GII* > 0.2 when the structure is unstable or has been assigned an incorrect space group (Brown 1992; Salinas-Sanchez et al. 1992; Wills and Brown 1999). The large *GII* value for CaIrO₃ at ambient conditions might be considered consistent with observed metastability of the structure.

The ab initio structure solution of TaAgS₃ (*Cmc*2₁, space group 36) (Wada and Onoda 1990) was refuted (Marsh 1993) and the most recently reported TaAgS₃ structure (*Cmcm*, space group 63, CaIrO₃ structure-type) has large anisotropic displacement parameters for each ion (Kim et al. 1997). In view of the large residual bond strain found in space group *Cmcm* and previous work examining structure model trials of NaMgF₃ postperovskite (Martin et al. 2006b), we have chosen to investigate structure model trials of CaIrO₃ in space group *Cmc*2₁.

The CaIrO₃ structure models in space group *Cmc*2₁ derived from the neutron diffraction data at 2 K, 293(2) K, and 9.72(5) GPa are listed in Table 2. The *Cmc*2₁ structural models are very similar to those in space group *Cmcm*, yet all ions show consistent displacement from the (001) mirror plane. While fluctuations in atomic position above and below this mirror plane between trial structures would best characterize statistical noise, deviations from *Cmcm* are relatively small. In addition, goodness of fit and residual bond strain of structure models in space group *Cmc*2₁ is unchanged relative to refinements in space group *Cmcm*. Deviations from the *Cmcm* structure model, if they exist, are within experimental error, and our analysis of the data taken at high pressure is limited to the *Cmcm* structure model.

Rietveld structure refinement (Fig. 2) reveals structure changes in CaIrO₃ at high pressure (Table 3, Fig. 3). Using these data together with data collected at high temperature (Martin et al. 2007a), we may investigate structure mechanisms that drive axial compression and thermal expansion of the unit cell. Mechanisms changing perovskite-type structures are commonly defined in terms of octahedral tilt and bond length (Glazer 1972, 1975; Ross and Hazen 1989; Zhao et al. 1993, 2004). To describe mechanisms operating upon compression and expansion of the CaIrO₃ structure (ABX₃) we highlight relative changes in specific Ir-O bond lengths as well as the ratio of volume changes of iridium- and calcium-centered polyhedra (V_B and V_A). Because it is useful to compare V_A/V_B between perovskite and post-perovskite structures (ABX₃), it is important to note the V_A/V_B ratio does not depend on the formal coordination number of the A site (Thomas 1998) and has the same definition in both perovskite and postperovskite structure-types: all unit-cell volume not occupied by

the B-site octahedra is volume of the A site.

The volume change of the Ca^{2+} site dominates compression and thermal expansion of the unit-cell volume, thus, V_A/V_B increases with temperature (Martin et al. 2007a) and decreases with pressure (Fig. 4). Also, this suggests that the mechanism driving the small compressibility and large thermal expansion of the **c**-axis relative to the **a**-axis resides within the IrO_6 octahedra.

Octahedra in $CaIrO_3$-type structures are much more deformed (Martin et al. 2006b; Rodi and Babel 1965) than octahedra found within perovskite-type (Zhao et al. 1993) structures. It is useful to measure deformation relative to undistorted octahedra, in which all Ir-O distances are equal and all O-Ir-O angles are 90°. The deformation in IrO_6 octahedra is plotted as a function of increasing temperature (Martin et al. 2007a) and pressure in Figure 5. Labels for bonds in the $CaIrO_3$ structure correspond to the Wyckoff symbols for atom positions in the structure. The bond geometry of the Ca site is such that Ca-O_{8f}^b forms the bicaps to the trigonal prism, which has Ca-O_{8f}^a bonds at its base and Ca-O_{4c} bonds to the prism apex. To understand how Ir-O bond lengths drive changes in the unit cell, it is important to note that Ir-O_{4c} has unit-cell vector components in only **y** and **z** (**b** and **c** axes) and Ir-O_{8f} has significant unit-cell vector components in only **x** and **y** (**a** and **b** axes) (Fig. 1).

Ir-O and Ca-O bond lengths are shown as a function of pressure in Figure 6a. With increasing pressure all bond lengths decrease and less change is observed in Ir-O bonds than in Ca-O bonds. In contrast, with increasing temperature, bond lengths increase as well as decrease (Fig. 6b) and the mechanism driving low compressibility and high thermal expansion of the
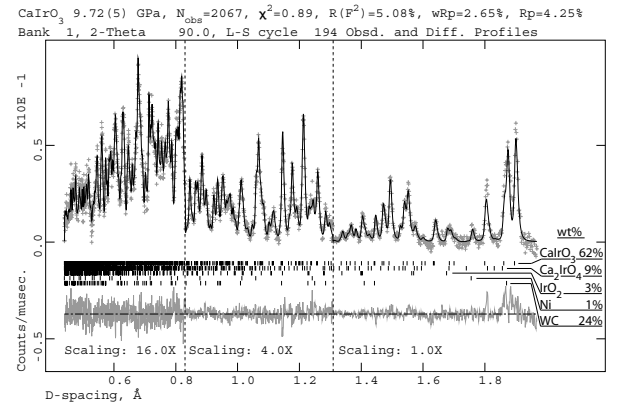
TABLE 2. Refined unit-cell parameters, atomic coordinates, isotropic temperature factors (U), and refinement statistics are listed for CaIrO₃ (Cmc2₁) structure model trials at room pressure and low temperatures [2.0(1) and 293(2) K] with a trial at high pressure and room temperature [9.72(5) GPa]

Conditions	293(2) K	2.0(1) K	9.72(5) GPa
a (Å)	3.13642(6)	3.13450(9)	3.1010(4)
b	9.88337(20)	9.87576(27)	9.6588(13)
c	7.29891(13)	7.29521(18)	7.2111(9)
V (Å³)	226.255(8)	225.827(10)	215.99(5)
Ca[4a]			
y	0.25049(13)	0.25028(14)	0.2467(5)
z	−0.0100(14)	−0.0130(9)	−0.0051(24)
U (Å²·100)	0.542(15)	0.163(16)	1.09(8)
Ir[4a]			
y	0.00141(25)	0.0002(5)	0.0046(6)
z	0.2382(6)	0.2390(5)	0.2418(14)
U	0.221(7)	0.114(6)	0.73(4)
O[4a] (i)			
y	0.92506(10)	0.92547(12)	0.9228(5)
z	−0.0083(11)	−0.00793(71)	−0.0088(25)
U	0.361(8)	0.183(8)	1.05(4)
O[4a] (ii)			
y	0.62985(31)	0.62873(44)	0.6304(13)
z	0.1910(4)	0.19165(36)	0.1868(12)
U	0.361(8)	0.183(8)	1.05(4)
O[4a] (iii)			
y	0.62443(31)	0.62505(44)	0.6289(12)
z	0.7915(4)	0.79271(34)	0.7876(13)
U	0.361(8)	0.183(8)	1.05(4)
χ^2	1.785	1.469	0.882
wR_p	2.09%	0.78%	2.63%
R_p	6.16%	2.35%	4.24%

Notes: Ca = 0, y, z; Ir = 0, y, z; O₄ₐ = 0, y, z.

FIGURE 2. Rietveld structure refinement of CaIrO₃ showing the fit to the data collected at 9.72(5) GPa. Data below 1.3 Å d-spacing are magnified (counts-scale) by a factor of 4, while the intensities below 0.82 Å are magnified by a factor of 16. Weight fraction of each phase is refined and included in the plot at this pressure.
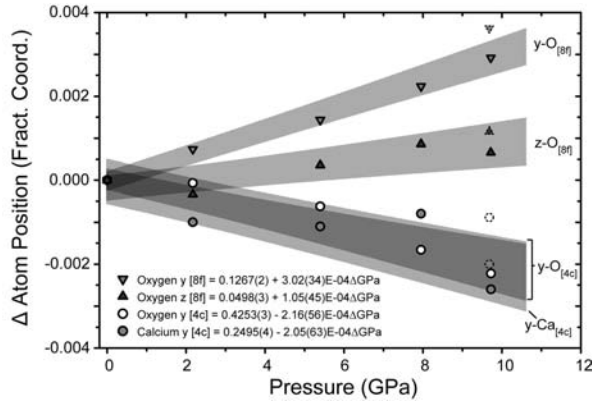
TABLE 3. Refined unit-cell parameters, positional parameters, isotropic temperature factors (U), and refinement statistics are listed for CaIrO₃ (Cmcm) at high pressure

Presssure (GPa)	0.00(5), V_O	2.17(5)	5.40(5)	7.95(5)	9.72(5)	9.68(8)*
Oil bars to press	70	250	500	700	800	850
a (Å)	3.14341(35)	3.1332(4)	3.1193(4)	3.1084(4)	3.1011(4)	3.1015(4)
b	9.8816(11)	9.8271(14)	9.7505(13)	9.6931(14)	9.6587(13)	9.6551(14)
c	7.3021(8)	7.2805(10)	7.2496(9)	7.2280(10)	7.2111(9)	7.2141(10)
V (Å³)	226.82(4)	224.17(5)	220.49(5)	217.78(5)	215.99(5)	216.03(5)
Ca						
y	0.2496(5)	0.2486(6)	0.2485(5)	0.2488(6)	0.2470(5)	0.2476(6)
U (Å²·100)	1.45(7)	1.36(8)	0.90(4)	0.83(4)	0.81(4)	0.93(4)
Ir						
U	1.033(31)	0.94(4)	1.28(7)	1.26(7)	1.07(6)	1.12(7)
O[4c]						
y	0.42512(42)	0.42505(53)	0.42450(50)	0.42346(52)	0.42290(47)	0.42423(54)
U	1.44(6)	1.36(8)	1.24(7)	1.25(7)	1.05(6)	1.26(7)
O[8f]						
y	0.12673(26)	0.12747(31)	0.12817(30)	0.12897(31)	0.12965(29)	0.13035(30)
z	0.04994(34)	0.0496(4)	0.0503(4)	0.0508(4)	0.0506(4)	0.0511(4)
U	1.26(5)	1.05(5)	1.05(5)	1.03(5)	0.98(5)	0.86(5)
χ^2	0.8625	0.8563	0.8919	0.9177	0.8897	0.9236
wR_p	2.77%	3.38%	3.04%	2.95%	2.65%	2.94%
R_p	4.32%	4.86%	4.84%	4.45%	4.25%	4.78%

* 850 oil bar pressure considered quasi-hydrostatic sample pressure.

FIGURE 3. The change in atom positional parameters, in fractional coordinates, plotted as a function of pressure. The asymmetric unit of the CaIrO₃ structure model in space group *Cmcm* has 4 independent atomic positional parameters and each is normalized according to the "room pressure" value (70 oil bar). Error bars are larger than symbol size and are not shown for clarity. Each parameter, with standard deviation, has been fitted according to the linear equation displayed within the plot. Quasi-hydrostatic data (850 bar) are shown as symbols with dotted line. Equations refer to the real atomic position within the unit cell (Ca = 0, y, 0; Ir = 0, 0, 0; O_{4c} = 0, y, 0.25; O_{8f} = 0, y, z).
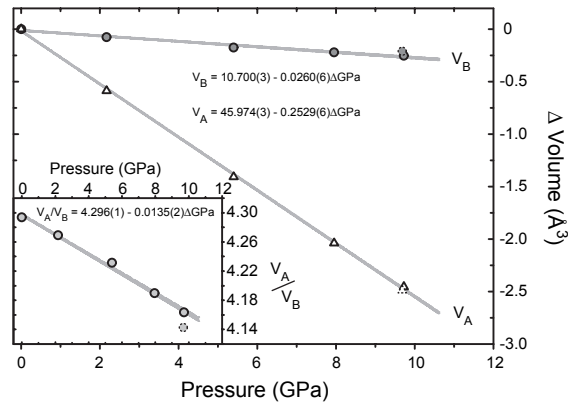
FIGURE 4. The volume of the Ca polyhedra (V_A), IrO₆ octahedra (V_B), and V_A/V_B ratio (inset) derived from Rietveld refinement are plotted as a function of pressure. Error bars are smaller than symbol size and each parameter, with standard deviation, has been fitted according to the linear equation displayed within the figure. Quasi-hydrostatic data (850 bar) are shown as symbols with dotted line. $V_A/V_B = [(V_{UC}/4) - V_B]/V_B$.

c-axis [001] relative to the **a**-axis [100] can be understood in these terms: Because Ir-O$_{4c}$ shows strong thermal expansion (components in only **b** and **c**), while Ir-O$_{8f}$ contracts (significant components in only **a** and **b**), the Ir-O vector components sum to increase [001] relative to [100] and $\alpha_c > \alpha_a$. At high pressure however, rather uniform bond compression decreases [100] relative to [001] and $\beta_a > \beta_c$. The relative axial sensitivities are not preserved since Ir-O$_{8f}$ bonds would need to expand (or resist compression) at high pressure for $\beta_c > \beta_a$.

In diffraction studies, the bond length is computed from the distance between maxima in the atomic distribution at any two given sites in the crystal. Corrections can be applied to overcome
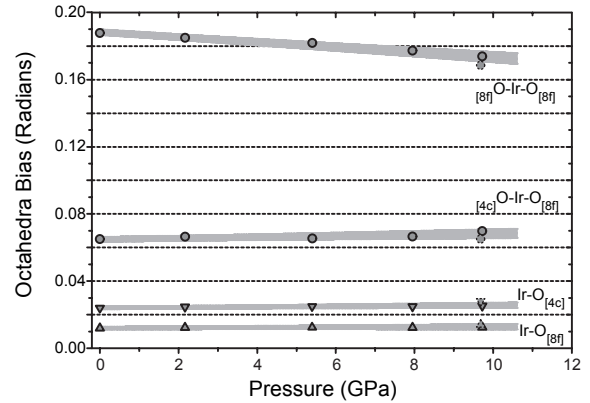

FIGURE 5. Deformation of IrO₆ octahedra as bias from a perfect octahedra is plotted as a function of pressure. Quasi-hydrostatic data (850 bar) are shown as symbols with dotted line. Ir-O bias = [(Ir-O) – (Ir-O)$_m$] /(Ir-O)$_m$, while O-Ir-O bias = tan [(π/2) – (O-Ir-O)].

possible artifacts driven by thermal motion, allowing approximation of real bond lengths within a crystal at high temperature (Busing and Levy 1964). In this correction, a correlation between the vibrating atoms must be assumed and we are reluctant to do so here when bond lengths are uniquely defined by the pair distribution function (Chapman et al. 2005; Chupas et al. 2004; Martin et al. 2007b; Qiu et al. 2005) and that describing CaIrO₃ at high temperature has yet to be examined. However, after correcting the observed bond lengths for thermal motion following Busing and Levy (1964), we can calculate the upper (R_U) and lower (R_L) bounds of this approximation,

$$R_U = R_{ij} + \frac{\left(\sqrt{U_i} + \sqrt{U_j}\right)^2}{2R_{ij}}$$

$$R_L = R_{ij} + \frac{\left(\sqrt{U_i} - \sqrt{U_j}\right)^2}{2R_{ij}}$$

where R_{ij} is the observed length between atoms i and j, while U_i and U_j are the isotropic mean-square displacements (units Å²) of atoms i and j from the crystallographic site. Considering the upper limit for the bond length approximation and the maximum isotropic mean-square displacements of each atom within uncertainty (Martin et al. 2007a),

$$U_{Ca} = 0.479(29) \cdot 10^{-2} + T \cdot 2.02(19) \cdot 10^{-5} - T^2 \cdot 8.4(26) \cdot 10^{-9}$$

$$U_{Ir} = 0.112(5) \cdot 10^{-2} + T \cdot 7.99(35) \cdot 10^{-6} - T^2 \cdot 4.6(47) \cdot 10^{-10}$$

$$U_O = 0.318(52) \cdot 10^{-2} + T \cdot 1.50(34) \cdot 10^{-5} - T^2 \cdot 6.0(453) \cdot 10^{-10}$$

the corrected Ir-O$_{8f}$ and Ca-O$_{4c}$ bond lengths change at a rate of –5.15·10⁻⁶ and –1.45·10⁻⁵(Å/K), respectively. Therefore, it appears that thermal motion cannot account for all of the observed reduction.

CONCLUDING REMARKS

The CaIrO₃ structure-type is rarely observed in ionic crystals and pressure is required to prevent amorphization and back-transformation of post-perovskite structured materials (Hirose et al. 2005; Kubo et al. 2006; Liu et al. 2005; Martin et al. 2006a; Murakami et al. 2004; Oganov and Ono 2004; Ono and Ohishi
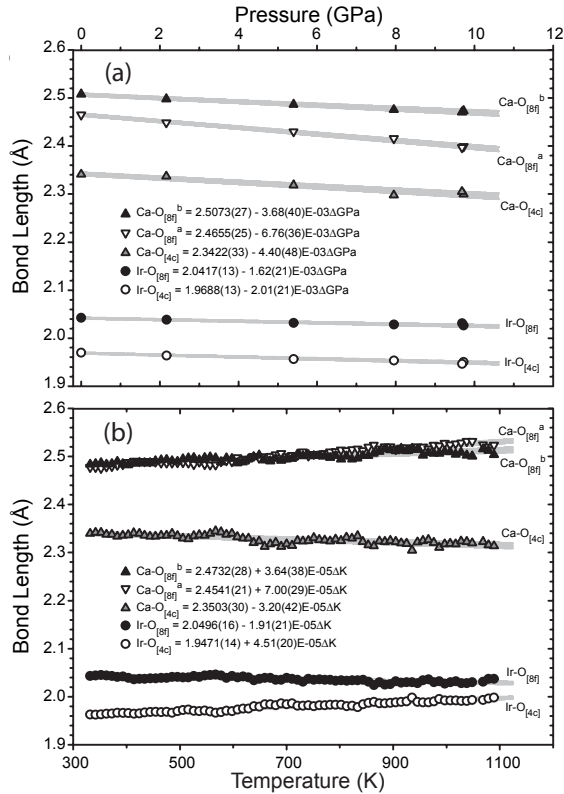
FIGURE 6. (**a**) Bond lengths within the CaIrO₃ structure plotted as a function of pressure and (**b**) as a function of temperature. Error bars are of the order of the symbol size and each parameter, with standard deviation, has been fitted according to the linear equation displayed within the figure.

2005; Santillan et al. 2006; Tateno et al. 2006). This observation is understood considering the shared octahedral edges along [100] in CaIrO₃-type structures and is consistent with pressure increasing overlap of the electron orbitals involved in bonding, leading to more covalent bonding in crystals. Pauling's third rule (Pauling 1929) states, due to cation-cation repulsion in ionic crystals, edge-sharing polyhedra are less stable than corner-sharing polyhedra. Electronic structure modeling of ilmenite $Na^{+1}Sb^{+5}O_3$ finds covalent bonding (Sb-O, Sb ns, O 2p), stabilizes edge-sharing SbO_6 octahedra relative to perovskite structure, where bonding within corner-sharing octahedra have a strong ionic character (Mizoguchi et al. 2004). Considering that covalent bonding is expected in all the CaIrO₃-type structures that are stable at room pressure [$UFeS_3$, $TlPbI_3$, $UScS_3$, $CaInBr_3$, $TaAgS_3$, (Berndt 1997)], perhaps we may expect bonding in post-perovskite MgSiO₃ to have a more covalent character and melting of a post-perovskite structure at higher temperatures than a perovskite-structured phase.

Results presented in this report show that pressure and temperature drive separate structural changes in CaIrO₃, thus the relative axial compressibility ($\beta_b > \beta_a > \beta_c$) and thermal expansion ($\alpha_b > \alpha_c > \alpha_a$) of the unit cell will change under simultaneous high pressure and temperature. Because α_c is large at room pressure, we might expect $\beta_c > \beta_a$ at sufficiently high temperatures where thermal effects may soften [001] at high pressure. If this is true,

the elastic constants of CaIrO₃ at room temperature or below could be significantly different from those at high temperature at any given pressure.

The CaIrO₃ structure changes through deformation of coordination units, rather than tilting of nearly rigid octahedra, which takes place in perovskite structures. Increasing the tilt of perovskite octahedra (e.g., Angel et al. 2005; Liu et al. 2005) drives the structural phase transition to the post-perovskite structure (CaIrO₃-type) by decreasing V_A/V_B. Considering V_A/V_B is greater than 4 in perovskite structures, while less than ~4 in post-perovskite structures, the pressure-temperature region of perovskite/post-perovskite phase transition can be predicted based on extrapolation of V_A/V_B. Assuming the phase transition between CaIrO₃ and perovskite-type CaIrO₃ occurs at a constant V_A/V_B everywhere in pressure-temperature space, we can use our experimental values $\partial P/\partial(V_A/V_B) = 74\,070(1100)$ MPa/(V_A/V_B), and $\partial T/\partial(V_A/V_B) = 4901(360)$ °C/(V_A/V_B) (Martin et al. 2007a) to calculate a Clapeyron slope of 15(3) MPa/°C for the phase transition. This calculated value is in remarkable agreement with the experimentally determined value 17(3) MPa/°C (Hirose and Fujita 2005). However, we believe this number should not describe the Clapeyron slope of the phase transition in MgSiO₃ rather, we conclude it may be possible to estimate the Clapeyron slope between perovskite/post-perovskite phases of MgSiO₃ when $\partial P/\partial(V_A/V_B)$ and $\partial T/\partial(V_A/V_B)$ are experimentally determined for this material.

Although V_A/V_B appears useful for predicting the phase transition between perovskite and post-perovskite structure, V_A/V_B implies a measure of relative ion valence between the two cation sites. Considering all CaIrO₃-type structures have very similar V_A/V_B ratios, we should expect cations in CaIrO₃-type structures of Fe_2O_3 and Mn_2O_3 to be 2^+ and 4^+ rather than 3^+ and 3^+ (Ono and Ohishi 2005; Santillan et al. 2006). This observation implies a 4^+ oxidation state of Fe is stabilized in these high pressure structures. If Fe^{4+} were to exist in the lower mantle, perhaps we could expect iron to occupy both magnesium and silicon sites in MgSiO₃ post-perovskite during solid-solution and/or stabilization of a CaIrO₃-type MgFeO₃ structure.

REFERENCES CITED

Angel, R.J., Zhao, J., and Ross, N.L. (2005) General rules for predicting phase transitions in perovskites due to octahedral tilting. Physical Review Letters, 95, 025503.
Berndt, M. (1997) ICSC/RETRIEVE 2.01 Crystal Structure Database. Gmelin Institute/FIZ Karlsruhe, Germany.
Brown, I.D. (1992) Chemical and steric constraints in inorganic solids. Acta Crystallographica Section B—Structural Science, 48, 553–572.
Brown, I.D. and Altermatt, D. (1985) Bond-valence parameters obtained from a systematic analysis of the inorganic crystal-structure database. Acta Crystallographica Section B-Structural Science, 41, 244–247.
Brown, I.D. and Shannon, R.D. (1973) Empirical bond-strength bond-length curves for oxides. Acta Crystallographica Section A, 29, 266–282.
Busing, W.R. and Levy, H.A. (1964) Effect of thermal motion on estimation of bond lengths from diffraction measurements. Acta Crystallographica, 17, 142–146.
Chapman, K.W., Chupas, P.J., and Kepert, C.J. (2005) Direct observation of a transverse vibrational mechanism for negative thermal expansion in Zn(CN)₂:

An atomic pair distribution function analysis. Journal of the American Chemical Society, 127, 15630–15636

Chupas, P.J., Chaudhuri, S., Hanson, J.C., Qiu, X.Y., Lee, P.L., Shastri, S.D., Billinge, S.J.L., and Grey, C.P. (2004) Probing local and long-range structure simultaneously: An in situ study of the high-temperature phase transition of alpha-AlF₃. Journal of the American Chemical Society, 126, 4756–4757.

Eichler, B., Zude, F., Fan, W., Trautmann, N., and Herrmann, G. (1993) Complex transport reactions in a temperature-gradient tube—radiochemical study of volatilization and deposition of iridium oxides and hydroxides. Radiochimica Acta, 61, 81–90.

Garnero, E.J. (2004) A new paradigm for Earth's core-mantle boundary. Science, 304(5672), 834–836, DOI: 10.1126/science.1097849.

Glazer, A.M. (1972) Classification of tilted octahedra in perovskites. Acta Crystallographica Section B-Structural Science, B28, 3384–3392.

——— (1975) Simple ways of determining perovskite structures. Acta Crystallographica Section A, 31, 756–762.

Goodman, L. (1960) On the exact variance of products. Journal of the American Statistical Association, 55, 708–713.

Hirose, K. (2006) Postperovskite phase transition and its geophysical implications. Reviews of Geophysics, 44, RG3001.

Hirose, K. and Fujita, Y. (2005) Clapeyron slope of the post-perovskite phase transition in CaIrO₃. Geophysical Research Letters, 32, L13313, DOI:10.1029/2005GL023219.

Hirose, K., Kawamura, K., Ohishi, Y., Tateno, S., and Sata, N. (2005) Stability and equation of state of MgGeO₃ post-perovskite phase. American Mineralogist, 90, 262–265.

Hull, S., Smith, R.I., David, W.I.F., Hannon, A.C., Mayers, J., and Cywinski, R. (1992) The POLARIS powder diffractometer at ISIS. Physica B: Physics of Condensed Matter, 180, 1000–1002.

Kim, C., Yun, H.S., Lee, Y., Shin, H., and Liou, K. (1997) Structure and electrical conductivity of AgTaS₃. Journal of Solid State Chemistry, 132, 389–393.

Kubo, A., Kiefer, B., Shen, G.Y., Prakapenka, V.B., Cava, R.J., and Duffy, T.S. (2006) Stability and equation of state of the post-perovskite phase in MgGeO₃ to 2 Mbar. Geophysical Research Letters, 33, L12S12, DOI:10.1029/2006GL025686.

Larson, A.C. and Von Dreele, R.B. (2000) General Structure Analysis System (GSAS). Los Alamos National Laboratory Report, 86–748.

Lay, T., Williams, Q., and Garnero, E.J. (1998) The core-mantle boundary layer and deep Earth dynamics. Nature, 392, 461–468, DOI: 10.1038/33083.

Lay, T., Garnero, E.J., and Williams, Q. (2004) Partial melting in a thermo-chemical boundary layer at the base of the mantle. Physics of the Earth and Planetary Interiors, 146, 441–467.

Lay, T., Hernlund, J., Garnero, E.J., and Thorne, M.S. (2006) A post-perovskite lens and D″ heat flux beneath the central Pacific. Science, 314, 1272–1276.

Liu, H.Z., Chen, J., Hu, J., Martin, C.D., Weidner, D.J., Hausermann, D., and Mao, H.K. (2005) Octahedral tilting evolution and phase transition in orthorhombic NaMgF₃ perovskite under pressure. Geophysical Research Letters, 32, L04304, DOI:10.1029/2004GL022068.

Mao, L.W., Mao, H.K., Sturhahn, W., Zhao, J., Prakapenka, V.B., Meng, Y., Shu, J.F., Fei, Y.W., and Hemley, R.J. (2006) Iron-rich post-perovskite and the origin of ultralow-velocity zones. Science, 312, 564–565, DOI: 10.1126/science.1123442.

Marsh, R.E. (1993) The space group of AgTaS₃. Journal of Solid State Chemistry, 102, 282–283.

Marshall, W.G. and Francis, D.J. (2002) Attainment of near-hydrostatic compression conditions using the Paris-Edinburgh cell. Journal of Applied Crystallography, 35, 122–125.

Martin, C.D., Crichton, W.A., Liu, H.Z., Prakapenka, V., Chen, J.H., and Parise, J.B. (2006a) Phase transitions and compressibility of NaMgF₃ (Neighborite) in perovskite- and post-perovskite-related structures. Geophysical Research Letters, 33, L11305, DOI: 10.1029/2006GL026150.

——— (2006b) In-situ Rietveld structure refinement of perovskite and post-perovskite phases of NaMgF₃ (Neighborite) at high pressures. American Mineralogist, 91, 1703–1706.

Martin, C.D., Chapman, K.W., Chupas, P.J., Prakapenka, V.B., Lee, P.L., Shastri, S.D., and Parise, J.B. (2007a) Compression, thermal expansion, structure, and instability of CaIrO₃, the structure model of MgSiO₃ post-perovskite. American Mineralogist, 92, 1048–1053.

Martin, C.D., Chupas, P.J., Chapman, K.W., and Parise, J.B. (2007b) Local vs. average structure; a study of Neighborite (NaMgF₃) utilizing the pair-distribution function for quantitative structure determination. Journal of Applied Crystallography, 40, 441–448.

McDaniel, C.L. and Schneider, S.J. (1972) Phase relations in CaO-IrO₂-Ir system

in air. Journal of Solid State Chemistry, 4, 275–280.

Megaw, H.D. (1971) Crystal structures and thermal expansion. Materials Research Bulletin, 6, 1007–1018.

Merkel, S., Kubo, A., Miyagi, L., Speziale, S., Duffy, T.S., Mao, H.K., and Wenk, H.R. (2006) Plastic deformation of MgGeO₃ post-perovskite at lower mantle pressures. Science, 311, 644–646, DOI: 10.1126/science.1121808.

Mizoguchi, H., Woodward, P.M., Byeon, S.H., and Parise, J.B. (2004) Polymorphism in NaSbO₃: Structure and bonding in metal oxides. Journal of the American Chemical Society, 126, 3175–3184.

Murakami, M., Hirose, K., Kawamura, K., Sata, N., and Ohishi, Y. (2004) Post-perovskite phase transition in MgSiO₃. Science, 304, 855–858, DOI: 10.1126/science.1095932.

Oganov, A.R. and Ono, S. (2004) Theoretical and experimental evidence for a post-perovskite phase of MgSiO₃ in Earth's D″ layer. Nature, 430, 445–448, DOI: 10.1038/nature02701.

Ono, S. and Ohishi, Y. (2005) In situ X-ray observation of phase transformation in Fe₂O₃ at high pressures and high temperatures. Journal of Physics and Chemistry of Solids, 66, 1714–1720, DOI: 10.1016/j.jpcs.2005.06.010.

Pauling, L. (1929) The principles determining the structure of complex ionic crystals. Journal of the American Chemical Society, 51, 1010–1026.

Qiu, X.Y., Proffen, T., Mitchell, J.F., and Billinge, S.J.L. (2005) Orbital correlations in the pseudocubic O and rhombohedral R phases of LaMnO₃. Physical Review Letters, 94, 177–203.

Rodi, F. and Babel, D. (1965) Ternare Oxide Der Ubergangsmetalle .4. Erdalkali-iridium(4)-Oxide—Kristallstruktur Von CaIrO₃. Zeitschrift Fur Anorganische Und Allgemeine Chemie, 336, 17.

Ross, N.L. and Hazen, R.M. (1989) Single-crystal X-ray-diffraction study of MgSiO₃ perovskite from 77 to 400 K. Physics and Chemistry of Minerals, 16, 415–420.

Salinas-Sanchez, A., Garcia-Munoz, J.L., Rodriguez-Carvajal, J., Saez-Puche, R., and Martinez, J.L. (1992) Structural characterization of R₂BaCuO₅ (R = Y, Lu, Yb, Tm, Er, Ho, Dy, Gd, Eu and Sm) oxides by X-ray and neutron-diffraction. Journal of Solid State Chemistry, 100, 201–211.

Santillan, J., Shim, S.H., Shen, G.Y., and Prakapenka, V.B. (2006) High-pressure phase transition in Mn₂O₃: Application for the crystal structure and preferred orientation of the CaIrO₃ type. Geophysical Research Letters, 33, L15307.

Shieh, S.R., Duffy, T.S., Kubo, A., Shen, G.Y., Prakapenka, V.B., Sata, N., Hirose, K., and Ohishi, Y. (2006) Equation of state of the postperovskite phase synthesized from a natural (Mg,Fe)SiO₃ orthopyroxene. Proceedings of the National Academy of Sciences of the United States of America, 103(9), 3039–3043.

Sinmyo, R., Hirose, K., O'Neill, H.St.C., and Okunishi, E. (2006) Ferric iron in Al-bearing post-perovskite. Geophysical Research Letters, 33, L12S13, DOI:10.1029/2006GL025858.

Spera, F.J., Yuen, D.A., and Giles, G. (2006) Tradeoffs in chemical and thermal variations in the post-perovskite phase transition: Mixed phase regions in the deep lower mantle? Physics of the Earth and Planetary Interiors, 159, 234–246.

Stixrude, L. and Karki, B. (2005) Structure and freezing of MgSiO₃ liquid in Earth's lower mantle. Science, 310, 297–299, DOI: 10.1126/science.1116952.

Tateno, S., Hirose, K., Sata, N., and Ohishi, Y. (2006) High-pressure behavior of MnGeO₃ and CdGeO₃ perovskites and the post-perovskite phase transition. Physics and Chemistry of Minerals, 32, 721–725, DOI: 10.1007/s00269–005–0049–7.

Thomas, N.W. (1998) New global parameterization of perovskite structures. Acta Crystallographica Section B-Structural Science, 54, 585–599.

Toby, B.H. (2001) EXPGUI, a graphical user interface for GSAS. Journal of Applied Crystallography, 34, 210–213.

Tsuchiya, J., Tsuchiya, T., and Wentzcovitch, R.M. (2005) Vibrational and thermodynamic properties of MgSiO₃ postperovskite. Journal of Geophysical Research-Solid Earth, 110, B02204, DOI: 10.1029/2004JB003409.

Wada, H., and Onoda, M. (1990) Preparation of new compound AgTaS₃. Chemistry Letters, 5, 705–706.

Wills, A.S. and Brown, I.D. (1999) VaList, CEA, France

Zhao, Y.S., Weidner, D.J., Parise, J.B., and Cox, D.E. (1993) Thermal-expansion and structural distortion of perovskite—data for NaMgF₃ perovskite. 1. Physics of the Earth and Planetary Interiors, 76, 1–16.

Zhao, J., Ross, N.L., and Angel, R.J. (2004) Tilting and distortion of CaSnO₃ perovskite to 7 GPa determined from single-crystal X-ray diffraction. Physics and Chemistry of Minerals, 31, 299–305.